Hemispherical-Directional Reflectance (HDRF) of Windblown Snow-Covered Arctic Tundra at Large Solar Zenith Angles

Christopher P. Ball, *Member, IEEE*, Amelia A. Marks, Paul D. Green, Alasdair MacArthur, Marion Maturilli, Nigel P. Fox, and Martin D. King

***Abstract*—Ground-based measurements of the hemispherical-directional reflectance factor (HDRF) of windblown snow-covered Arctic tundra were measured at large solar zenith angles (79°–85°) for six sites near the international research base in Ny-Ålesund, Svalbard. Measurements were made with the Gonio RAdiometric Spectrometer System over the viewing angles 0°–50° and the azimuth angles 0°–360°, for the wavelength range 400–1700 nm. The HDRF measurements showed good consistency between sites for near-nadir and backward viewing angles, with a relative standard deviation of less than 10% between sites where the snowpack was smooth and the snow depth was greater than 40 cm. The averaged HDRF showed good symmetry with respect to the solar principal plane and exhibited a forward scattering peak that was strongly wavelength dependent, with greater than a factor of 2 increase in the ratio of maximum to minimum HDRF values for all viewing angles over the wavelength range 400–1300 nm. The angular effects on the HDRF had minimal influence for viewing angles less than 15° in the backward viewing direction for the averaged sites and agreed well with another study of snow HDRF for infrared wavelengths, but showed differences of up to 0.24 in the HDRF for visible wavelengths owing to light-absorbing impurities measured in the snowpack. The site that had the largest roughness elements showed the strongest anisotropy in the HDRF, a large reduction in forward scattering, and a strong asymmetry with respect to the solar principal plane.**

***Index Terms*—Albedo, bidirectional reflectance distribution function (BRDF), black carbon, calibration, goniometer, hemispherical-conical reflectance factor (HCRF), hemispherical-directional reflectance factor (HDRF), reflectance, remote sensing, scattering, snow, surface roughness.**

I. Introduction

SPECTRAL surface albedo is the bihemispherical reflectance at a particular wavelength or the ratio of reflected radiant flux to the incident radiant flux of hemispherical angular extent [1]. The albedo of Arctic snow can be in excess of 0.9 for ultraviolet and visible wavelengths [2]. As a critical component in the global radiation budget, albedo defines the proportion of solar radiation absorbed, as well as reflected, over a large part of the Earth's surface [3], [4]. Sensors aboard Earth observing satellites have the unique ability to monitor the albedo of snow over remote and inaccessible regions such as the Arctic at high spatial and temporal resolution [5]–[7]. However, spaceborne sensors subtend only a discrete angle to the target surface, and the directional reflectance of snow is not isotropic [8], [9]. Furthermore, the reflectance of snow depends on the wavelength of the reflected radiation, and the majority of satellite sensors measure radiance over a limited number of spectral bands that are not always consistent from sensor to sensor. Consequently, satellite sensors require knowledge of the spectrally resolved bidirectional reflectance (BRDF) of the target surface to accurately derive climatically important surface properties such as surface albedo [10].

The accuracy to which satellite sensors are able to derive snow properties is dependent on the accuracy of the bidirectional reflectance distribution function (BRDF) model. To better build, test, and validate these models, hyperspectral ground-based directional reflectance data that are able to match the sensors spectral response are required. Several previous field studies have measured the hemispherical-directional reflectance (HDRF) of snow (e.g., [8], [9], and [11]–[16]). However, few studies have obtained measurements over rough windblown snow, or at very large solar zenith angles (greater than 80°), where satellite albedo retrieval algorithms are least reliable [5], [17] and where snow surface roughness has the greatest effect on reflectance [14], [18]. In addition, it has been shown that failure to account for snow surface roughness at large solar zenith angles in BRDF models can lead to order-of-magnitude errors in the derivation of snow surface properties [19]. Hence, more systematic measurements of snow directional reflectance for large solar zenith angles, as well as for a wider variety of snow surface types, are required [15].

Manuscript received February 6, 2014; revised October 14, 2014 and January 28, 2015; accepted March 16, 2015. Date of publication May 8, 2015; date of current version June 10, 2015. This work was supported by the National Physical Laboratory (NPL), the Natural Environment Research Council (NERC) under Grant NE/I018999/1, and Royal Holloway University of London Department of Earth Sciences.

C. P. Ball and M. D. King are with the Department of Earth Sciences, Royal Holloway, University of London, Surrey TW20 0EX, U.K. (e-mail: chris.ball.2007@live.rhul.ac.uk; m.king@es.rhul.ac.uk).

A. A. Marks was with Royal Holloway, University of London, Surrey TW20 0EX, U.K. She is now with the National Physical Laboratory, Teddington TW11 0LW, U.K. (e-mail: amelia.marks@npl.co.uk).

P. D. Green and N. P. Fox are with the National Physical Laboratory, Teddington TW11 0LW, U.K. (e-mail: paul.green@npl.co.uk; nigel.fox@npl.co.uk).

A. MacArthur is with the Natural Environment Research Council Field Spectroscopy Facility, School of Geosciences, The University of Edinburgh, Edinburgh EH9 2JW, U.K. (e-mail: alasdair.macarthur@ed.ac.uk).

M. Maturilli is with the Alfred Wegener Institute, Helmholtz Centre for Polar and Marine Research, 14473 Potsdam, Germany (e-mail: marion.maturilli@awi.de).

Color versions of one or more of the figures in this paper are available online at http://ieeexplore.ieee.org.

Digital Object Identifier 10.1109/TGRS.2015.2421733

The investigation described here measured the hemispherical-conical reflectance factor (HCRF) of windblown Arctic snow-covered tundra at six sites, typical of those seen across the Arctic region. The HCRF is the field measurable quantity where incoming irradiance from the entire hemisphere is considered alongside the reflected radiance [1]. The HCRF is dependent on the atmospheric conditions at the time of the measurement, as well as the topography and reflectance properties of the surrounding terrain. The HCRF measurements were made using the Gonio RAdiometric Spectrometer System (GRASS) [20] during a three-week field campaign in Ny-Ålesund, Svalbard, in Spring 2013. The goniometer's configuration allowed for an angular resolution of 10° in viewing angle and 30° in azimuth angle, covering the angular range of 0°–50° in zenith angles and 0°–360° in azimuth angles.

II. Theoretical Background and Definitions

Algorithms for the retrieval of surface albedo from satellite data require knowledge of the bidirectional reflectance of the Earth's surface [21]. The BRDF describes intrinsic reflectance properties of a surface, or the relationship between the incident light from a particular direction to the light reflected by the surface into a particular direction [22]. By definition, the BRDF is a ratio of infinitesimal quantities and cannot be measured directly as all field spectrometers have a finite field of view (FOV) [1], [23]. In addition, solar irradiance consists of both a direct term (nonscattered), and a diffuse term (scattered by clouds, aerosols, gases, and the surrounding terrain), the relative proportion of which is wavelength dependent [2], [24]. As a result, the measurable quantity in the field is the HCRF [1]. However, hereafter, the quantity measured in this study is referred to as the HDRF, as the HCRF is numerically equivalent to the HDRF under the assumption that the bidirectional reflectance over the solid angle subtended by the detector is isotropic [11], [12]. The HDRF is the radiance reflected by the target surface into a specified direction relative to the radiance reflected by a lossless Lambertian reflector into the same beam geometry under ambient illumination conditions [1], i.e.,

$$\mathrm{HDRF}(\theta_i, \phi_i, 2\pi; \theta_r, \phi_r; \lambda) = \frac{L_r(\theta_i, \phi_i, 2\pi; \theta_r, \phi_r; \lambda)}{L_{r,\mathrm{Lamb}}(\theta_i, \phi_i, 2\pi; \lambda)} \quad (1)$$

where L_r is the radiance reflected into the viewing azimuth angle ϕ_r and the viewing zenith angle θ_r, for a given radiance $L_{r,\mathrm{Lamb}}$ reflected by a lossless Lambertian reflector into the same beam geometry under ambient illumination conditions with a solar azimuth ϕ_i and solar zenith θ_i and where λ is the wavelength. The angles and quantities are schematically shown in Fig. 1. A detailed discussion of HCRF, HDRF, and BRDF is given by Schaepman-Strub *et al.* [1].

III. Methodology

The methodology will be divided into separate descriptions of the site, the goniometer, the laboratory testing of the goniometer, the field measurements, and the data reduction and processing procedures.

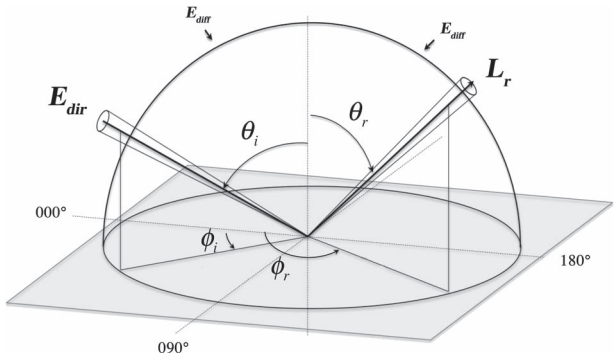

Fig. 1. Diagram of the angles and quantities required for defining the HDRF: E_{dir} is the irradiance from the azimuth direction (ϕ_i) and the zenith direction (θ_i), L_r is the measured radiance in the azimuth direction (ϕ_r) and the zenith direction (θ_r), and E_{diff} is the diffuse component to the irradiance.

Fig. 2. GRASS with 15 foreoptics mounted on three arms and one foreoptic positioned in the nadir view position. There is an integrating cosine irradiance collector mounted and leveled on the top of the structure. The spectrometer, multiplexer, and laptop are situated in the sled (left), and the all-sky camera is mounted and leveled on a tripod (out of view). Note that no measurement of HDRF was taken at the time this image was captured.

A. Experimental Site

Measurements of HDRF were carried out along two 100-m transects near the international research base in Ny-Ålesund (78° 55′ N, 11° 56′ E) in Svalbard in Spring 2013. The transects were located on two areas of undisturbed snow-covered tundra approximately 0.25 km east and 2.90 km north west of the Ny-Ålesund research base. The individual sites were systematically located at approximately 10-m intervals along each transect.

B. Instrumentation: GRASS

GRASS was used to measure the HDRF of the snow at each site during the field campaign.

1) Goniometer Design: GRASS has been developed at the U.K. National Physical Laboratory (NPL) in collaboration with the U.K. Natural Environment Research Council Field Spectroscopy Facility (NERC FSF) to measure the hemispherical-directional reflectance (HDRF) of natural surfaces [20], [25]. The goniometer was designed to be quickly assembled in

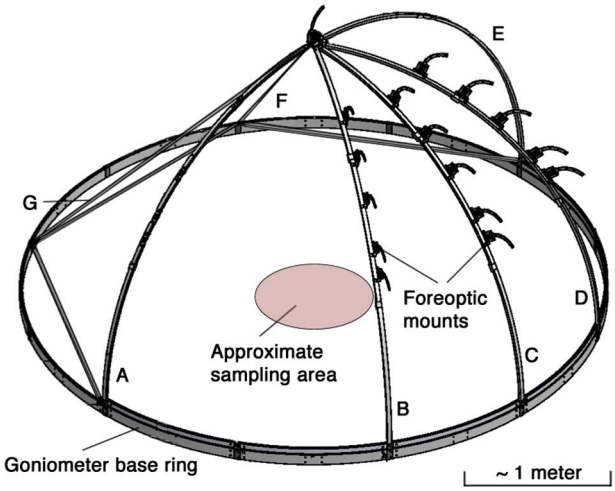

Fig. 3. Schematic of the goniometer's frame showing the relative position of each of the goniometer's arms (labeled A to G) and the approximate size of the sampling area (adapted from Pegrum *et al.* [25]). Note that the goniometer's arms can be manually rotated on top of the goniometer's base ring to prevent shadowing of the sampling area and to allow the sampling of radiance over a wide range of viewing azimuth angles.

remote situations and be robust and easily transportable. The structure consists of a series of vertical arms that form a hemispherical structure above the target surface (see Figs. 2 and 3). Fifteen foreoptics are mounted on three of the arms, and one foreoptic is located at the nadir view position at the top of the structure. For the configuration used here, each foreoptic was separated by 10° in viewing angle and approximately 30° in azimuth angle; the maximum viewing angle was 50°. The radius of the circular base of the structure is 2 m, as is the distance between each foreoptic and the goniometer's center point on the target surface. The goniometer arms were designed so that they can be manually rotated on the circular base of the structure to capture reflected sunlight over the full hemisphere; as such, three rotations of approximately 90° enabled GRASS to sample reflected radiance through 360° of azimuth at $\sim 30^\circ$ intervals. Each of the goniometer's foreoptics consists of an 8° (full angle) collimating lens coupled by optical fiber to a multiplexer that gives a single output to a dual-FOV visible to shortwave infrared (V-SWIR) spectroradiometer. A Labview program controls the operation of the multiplexer and the spectrometer, allowing GRASS to step through the optical input for each of the 16 foreoptics individually. An integrating cosine irradiance collector was attached to the top of the goniometer's frame and coupled to V-SWIR via a second input for a near-simultaneous measurement of total hemispherical (commonly known as "global") irradiance.

2) V-SWIR Spectrometer: V-SWIR utilizes two spectrometers, i.e., an Ocean Optics USB 2000+ and a B&W Tek sol 1.7, allowing for measurements over the wavelength range 400–1700 nm at 1-nm sampling interval. V-SWIR consists of a beam splitter to split the input light between the two spectrometers and a motorized mirror, which acts as an optical switch between the two inputs, allowing reflected radiance and global irradiance to be measured near simultaneously (separated by less than 2 s). The V-SWIR spectroradiometer is controlled by a laptop personal computer. Radiometric calibration of V-SWIR was carried out at NERC FSF prior to its use in the field using an integrating sphere source and a standard FEL lamp.

C. GRASS Laboratory Testing and Repeatability

Prior to its use in the field, the GRASS system underwent laboratory testing to assess the instrument's mechanical optical stability and pointing accuracy.

1) Mechanical Stability of the Optical System: The repeatability of the measurement setup upon rotating the goniometer's arms was tested in the laboratory at Royal Holloway, University of London (RHUL). The three arms were rotated on the circular base through eight rotations (each of approximately 90°), and the change in radiance recorded by the spectrometer was measured for each foreoptic and fiber while viewing an intensity-stabilized integrating sphere source. The integrating sphere source consisted of a tungsten halogen lamp, with a regulated and stabilized power supply, coupled to a Spectralon integrating sphere. The integrating sphere exit port surround was designed so that each foreoptic located in the same position in the integrating sphere, ensuring that the distance between the exit port aperture and the collimating lens was the same for each replicate measurement. The exit port of the integrating sphere was designed to snuggly surround each foreoptic to avoid any extraneous light contributing to the measurement. The relative standard deviation of the radiances recorded by the spectrometer between 400 and 1700 nm for all foreoptics and respective fibers over eight replicate measurements (excluding data from a single damaged fiber) was less than 5% (1σ) and was typically 2%.

2) Pointing Accuracy and Foreoptic Footprint Overlap: For polar fieldwork, the structure had to be lightweight, causing a loss of rigidity and a less-than-perfect footprint overlap for the individual foreoptics. The footprint overlap was assessed by measuring the pointing accuracy of the goniometer in a dark laboratory at RHUL. The spectrometer and the multiplexer were disconnected from the six foreoptics on the middle arm of the goniometer, and a diode laser was shone back down each optical fiber and foreoptic to illuminate an area of white linoleum flooring that represented the target surface. The illuminated area corresponds to the footprint of the HDRF measurement. The center point of the footprint was recorded by tracing the major and minor axes of the illuminated area. The positions of the footprint center points were recorded for the same viewing angles as used in the field study (0°–50°) and for four different azimuth positions ($0^\circ, 90^\circ, 180^\circ$, and 270°), a total of 24 different viewing positions. The size and shape of the footprint were calculated with the knowledge of the foreoptics FOV and the approximate distance to the goniometer's center point. The footprints and center points for the 24 view positions are plotted in Fig. 4.

The maximum distance of the foreoptic footprint center from the goniometer center was found to be 20.49 cm, implying a pointing accuracy of roughly ± 20 cm and an approximate sample area size of 0.4 m^2, which is not sampled fully or equally. At 50° viewing angle, the footprint had a major axis diameter of 47 cm, and at the nadir view position, the footprint

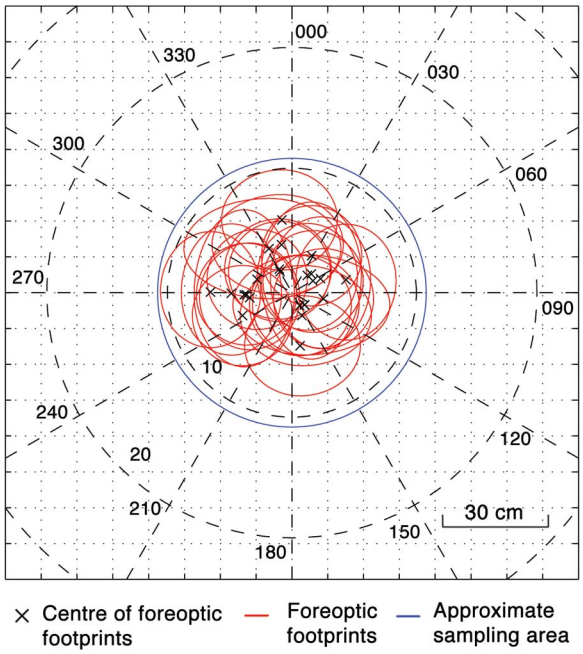

Fig. 4. Overlap of foreoptic footprints at six different viewing zenith positions (0°–50°) and at four different viewing azimuth positions (0°–270°).

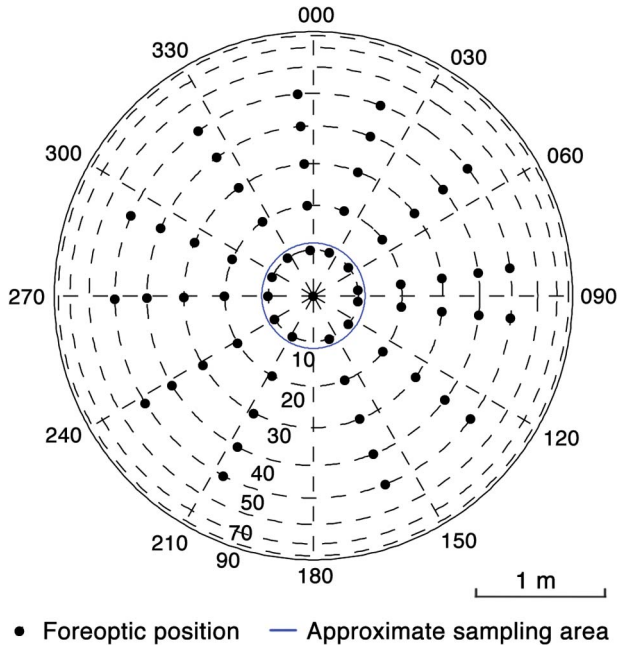

Fig. 5. Typical sampling positions of the GRASS foreoptics and the approximate size of the sampled area. The sunlight intersects the plot at the 180° index.

was circular and had a diameter of 28 cm. Given the relatively large footprint area, the pointing accuracy was considered satisfactory for sites where the snow surface was homogeneous. The impact of the imperfect footprint overlap for sites that were considered heterogeneous, owing to the presence of roughness elements, is discussed in Section III-E2.

D. Field Measurements

The following section describes the field HDRF measurements and the associated ancillary sky and snow measurements.

1) HDRF Acquisition: The HDRF of the snow surface at each site was measured using the GRASS system. Reflected radiance was recorded for each quarter of the hemisphere by the V-SWIR spectrometer. The arms holding the 16 foreoptics were manually rotated on the instruments base ring through each quarter of the hemisphere, and the azimuthal position of the arms was recorded. A schematic of the frame of the goniometer is given in Fig. 3.

The large diameter of the goniometer's base ring (4 m) compared with the diameter of the sampling area (0.8 m), combined with the ability to manually adjust the azimuthal positioning of the arms, allowed the goniometer's arms to be manually positioned so that there is no shadowing of the sampling area during the HDRF acquisition. Consequently, the foreoptics do not always measure radiance at equal intervals in azimuth angle (see Fig. 5), and no measurement could be taken in the backward direction in the solar principal plane. The distance between the base of arms A and B in Fig. 3 is 60°, or 1 m. The azimuth angle between the base of arms B and C is 30°, likewise for arms C and D. Fig. 5 illustrates a typical setup where the goniometer arms are positioned so that there is no shadowing of the target surface. The goniometer was leveled at each site by pressing the base ring into the snowpack, as shown in Fig. 2. The base ring of the goniometer is in the snowpack on the right-hand side of the image in Fig. 2 and is on top of the snowpack on the left-hand side of the image. The radiance reflected by a calibrated Spectralon reference panel placed on the snow surface at the end of each HDRF acquisition was measured using V-SWIR and the foreoptic at the nadir viewing position. An integration time of 2 s was necessary to achieve the required signal-to-noise ratio for V-SWIR, resulting in a typical total measurement time of approximately 60 min for a complete measurement of one target.

2) Foreoptic Intercalibration: Foreoptics and fibers were intercalibrated at each field site at the end of each HDRF acquisition to account for their respective transmission efficiencies. Variability in radiances was recorded as a function of wavelength for each individual foreoptic while viewing a stabilized integrating sphere source described in Section III-C1. Intercalibration correction factors were calculated by normalizing the radiance for each of the 15 foreoptics to the radiance recorded by the foreoptic at the nadir viewing position as follows:

$$C_f(\lambda) = \frac{L_{\mathrm{IS},f=\mathrm{nadir}}(\lambda)}{L_{\mathrm{IS},f}(\lambda)} \tag{2}$$

where C_f is the intercalibration correction factor for the foreoptic f, and $L_{\mathrm{IS},f=\mathrm{nadir}}$ is the radiance recorded by the spectrometer while viewing the intensity-stabilized integrating sphere source with the nadir foreoptic. $L_{\mathrm{IS},f}$ is the radiance recorded by the spectrometer while viewing the stable integrating sphere source with the foreoptic f. The choice of the nadir foreoptic as the reference is purely for convenience.

3) Spectralon Reference Panel: Equation (1) defines the HDRF as the ratio of radiance reflected by the target surface into a particular direction to that reflected by a lossless

TABLE I
LIST OF HDRF ACQUISITIONS AND SNOW PIT DATA

Site ID	Date of acquisition	Average solar zenith angle (°)	Grain size (mm)	Density (kg m^{-3})	Temperature (°C)	Total snow depth (cm)	Roughness scale: height/ wavelength (cm)	Max concentration of black carbon (ng g^{-1})
S1	20/03/13	85	1	322 ± 13	-14.2	57	< 1 / < 1	299 ± 72
S2	21/03/13	84	0.5	308 ± 23	-4.9	26	1 to 2 / 5 to 20	130 ± 31
S3	24/03/13	80	1.5	316 ± 10	-4.6	9	1 to 6 / 5 to 30	102 ± 24
S4	20/03/13	81	1	324 ± 21	-11.0	41	< 1 / < 1	238 ± 57
S5	01/04/13	79	1.5	272 ± 46	-10.8	49	< 1 / < 1	92 ± 22
S6	25/03/13	81	1	303 ± 22	-4.2	14	< 1 / < 1	192 ± 46

Grain size and temperature has been averaged for the top 10 cm of the snowpack. The uncertainty in the density and maximum black carbon measurements is calculated as one standard deviation of the replicate measurements.

Lambertian reflector under ambient illumination. A Spectralon panel viewed from nadir ($\theta_r = 0$) and positioned on the snow surface at the end of the measurement sequence was used to approximate a lossless Lambertian reflector. The Spectralon panel was calibrated at NPL, using the National Reference Reflectometer [26], [27] for the solar and view geometries used in the field to account for the departure of our panel from a lossless Lambertain reflector [28]. The calibration yielded a reflectance correction factor β for the wavelength range 400–1000 nm, which is defined as the ratio of the radiance reflected by the Spectralon panel in a given direction θ to that of a lossless Lambertian reflector identically irradiated [26], i.e.,

$$\beta = \frac{R(2s/d)^2}{\cos(\theta)} \tag{3}$$

where R is the measured ratio of reflected power to incident power, s is the distance between the sample surface and the detector's aperture, and d is the diameter of the aperture. The spectrally averaged value of β (0.88) was used, since the wavelength dependence over the range 400–1000 nm was found to be less than 0.5%. Correction factors were assumed to be valid up to 1700 nm as the wavelength dependence of the hemispherical reflectance of Spectralon (the average of seven panels), presented by Jackson *et al.* [29], was less than 1% over the wavelength range 1000–1700 nm.

The reflectance correction factor was measured with an incident beam angle of 0° zenith angle and a viewing angle of 80°. To obtain the approximate configuration used in the field, the directions were exchanged by applying the Helmholtz reciprocity principle [30]. The reflectance characteristics of the Spectralon panel were assumed to be rotationally symmetric to nadir [28]. Given that a Lambertian surface has a constant radiance independent of view angle, the radiance measured from nadir was applied to all other foreoptics when calculating the HDRF. The radiance reflected by the Spectralon panel was subject to correction by the intercalibration correction factor C_f derived in Section III-D2, when applied to each of the individual foreoptics. Temperature differences between ambient laboratory and field conditions were considered unlikely to significantly affect the reflectance of the Spectralon reference standard [31].

4) Calculating the HDRF: The HDRF is calculated here by combining (1), (2), and (3) as follows:

$$\mathrm{HDRF}(\theta_i, \phi_i, 2\pi; \theta_r, \phi_r; \lambda) = \frac{L_r(\theta_i, \phi_i, 2\pi; \theta_r, \phi_r; \lambda)}{L_{r,\mathrm{Spectralon}}(\theta_i, \phi_i, 2\pi; \lambda)} C_f(\lambda)\beta \tag{4}$$

where C_f is the foreoptic intercalibration correction factor defined in Section III-D2, and β is the reflectance correction factor for the Spectralon reference panel defined in Section III-D3. The measured HDRF function was then projected onto a 2-D grid and linearly interpolated using a Delaunay-triangle-based method [32].

The extent of anisotropy in the HDRF over all viewing angles can be described using the anisotropy index (ANIX) [12]

$$\mathrm{ANIX}(\lambda) = \frac{\max\left(\mathrm{HDRF}(\lambda)\right)}{\min\left(\mathrm{HDRF}(\lambda)\right)}. \tag{5}$$

5) Ancillary Sky Measurements: During the HDRF acquisition, ancillary measurements were made in order to characterize the sky conditions. All-sky camera imagery was acquired at 1-min intervals using a Nikon Coolpix E4500 digital camera and fish-eye lens. As part of the Baseline Surface Radiation Network, broadband shortwave global and diffuse radiation (200–3600 nm) is measured at 1-min intervals near the field site at the AWIPEV research station using a Kipp & Zonen CMP22 pyranometer. Measurements of aerosol optical thickness were made at the field site using a handheld Microtops II sunphotometer [33] at approximately 15-min intervals during each HDRF acquisition. The sunphotometer had five filters centered at 440, 675, 870, 936, and 1020 nm, with a full-width half-maxima of 10 nm and full FOV of 2.5°.

6) Analysis of Snowpack: At each site, snow pits were sampled at 5-cm-depth intervals to obtain measurements of snow depth, temperature, and grain size. The scale of the surface roughness at each site was estimated by measuring the height (the vertical distance between the trough and the peak) and the wavelength (the horizontal distance between two peaks) of the roughness elements. The snowpack was heavily reworked, and regular structures were difficult to identify; thus, a range of heights and wavelengths were recorded. The ranges are presented in Table I and are typical over the sampling area and

characteristic of the area surrounding the measurement. Grain size was recorded according to the international classification for seasonal snow on the ground [34] using a hand lens and crystal card. Snowpack density was measured in the top 10 cm, other than at S3, where snow was sampled from the top 9 cm owing to thin snow cover. The snow samples were collected by pressing three 240-ml wide-mouth polytetrafluoroethylene (PTFE) sample jars downward into the top of the snow surface and measuring the mass of snow samples. An upper limit on the mass ratio of black carbon in the top 10 cm of the snowpack was determined for each site by spectrophotometric analysis of the particulate matter retained on the filters. Snow samples for measuring the maximum mass ratio of black carbon in snow were collected from each snow pit by pressing a 240-ml wide-mouth PTFE sample jar horizontally into the top 10 cm of the snowpack. The samples were transported to the laboratory in Ny-Ålesund, where 1500 ml of melted snow was filtered through a 0.4-μm Nucleopore membrane filter according to the methodology described by Doherty *et al.* [35]. The filter papers were then sealed and transported to the laboratory at RHUL, where an integrating sandwich spectrometer was used to determine the maximum concentration of black carbon in the snow according to the technique described by Grenfell *et al.* [36]. The upper limit on the concentration of black carbon in the snowpack at each site was found to be large when compared with typical values in Svalbard [35], which is caused by the proximity of the field sites to the Ny-Ålesund research station. Data collected about the snowpack are presented in Table I.

E. Data Processing and Reduction Procedures

The following section describes the data processing and reduction procedures.

1) Diffuse Sky Irradiance: Even under clear-sky conditions, the HDRF does not equal the BRDF of the surface due to the presence of diffuse irradiance [2], [24]. The long atmospheric path length of light for large solar zenith angles results in increased scattering, particularly in the Rayleigh-scattering-dominated wavelength region (400–800 nm), making it impossible to measure the HDRF at these angles without a high proportion of diffuse irradiance being present. The sky conditions during each HDRF acquisition were recorded using a Nikon Coolpix E4500 digital camera and fish-eye lens. Only sites that showed clear-sky conditions with no cumulus cloud and less than 10% visible cirrus cloud cover during the HDRF acquisition were retained for analysis. The ratio of broadband diffuse irradiance to global irradiance (200–3600 nm) was recorded by a Kipp & Zonen CMP22 pyranometer at the AWIPEV research station and was on average less than 0.5 for the remaining sites during each the HDRF acquisition.

2) Spatial Resolution and Surface Roughness: Surface roughness of the target surface is an important parameter in the measurement of HDRF [14], [37]; to take a representative measurement, typical surface roughness elements, such as sastrugi and ripples, needed to be sampled. To test whether the footprint size and the goniometer's pointing accuracy were sufficient to sample a representative number of roughness elements, the ratio of shaded to sunlit areas within a circular footprint of 0.28-m diameter (the size of the footprint used in the field measurements) was compared with the ratio of shaded to sunlit areas for a footprint with a 1-m diameter. The size and shape of the shadows were computed for a 1.5-m^2 grid according to the solar geometry and the height sas_h and wavelength sas_λ of the roughness elements observed at the sites S2 and S3, by taking the middle value for each range (for site S2, $\mathrm{sas}_h = 1.5$ and $\mathrm{sas}_\lambda = 12.5$, and for site S3, $\mathrm{sas}_h = 3.5$ and $\mathrm{sas}_\lambda = 17.5$). For simplicity, the roughness elements were assumed to be regularly spaced linear ridges with vertical walls, as in Leroux and Fily [37]. The ratio of shaded to sunlit areas for each footprint size was calculated and averaged for 100 different positions around the center of the grid by varying the x and y coordinates of the footprint center point by up to ± 20 cm, to resemble the pointing accuracy of the goniometer. The relative difference between the averaged ratio with a footprint diameter of 0.28 m and the ratio with a footprint diameter of 1 m was 2.9% for S2 and 19.4% for S3. The relative standard deviation of the averaged ratio with a 0.28-m-diameter footprint was 2.6% for S2 and 25.2% for S3, implying that the nadir viewing foreoptic was sampling a representative portion of surface roughness for sites S2 and S3. However, given the irregular distribution and size of the roughness elements at S2 and S3, combined with the imperfect footprint overlap, the possibility of any foreoptic capturing an unrepresentative sample that causes errors in excess of what is estimated earlier could not be eliminated; as such, the sites where surface roughness features were observed were omitted from the final analysis, but are retained in the discussion section.

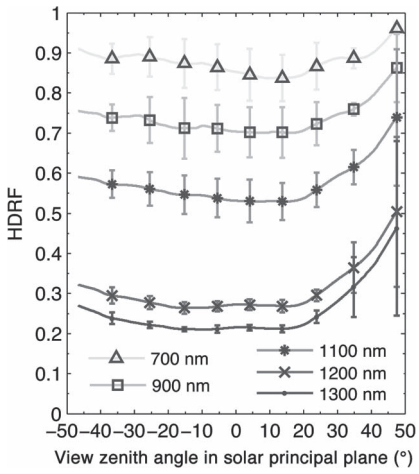

Fig. 6. Averaged HDRF for S1, S4, and S5 in the solar principal plane for sites where the snow surface was smooth and the snow depth was over 40 cm. The average solar zenith angle was 82°.

3) Change in Solar Zenith and Azimuth Angles: The measurement time for a single HDRF acquisition was typically 60 min, which, for the measurement location and time of year, corresponds to a change of approximately 3° in solar zenith angle and 16° in solar azimuth angle. To avoid geometric perturbations in the HDRF distribution due to changes in solar azimuth angle, the actual solar azimuth angle was determined for each radiance measurement during the HDRF acquisition. The solar azimuthal offset since the start of the measurement sequence for each radiance measurement was calculated, and

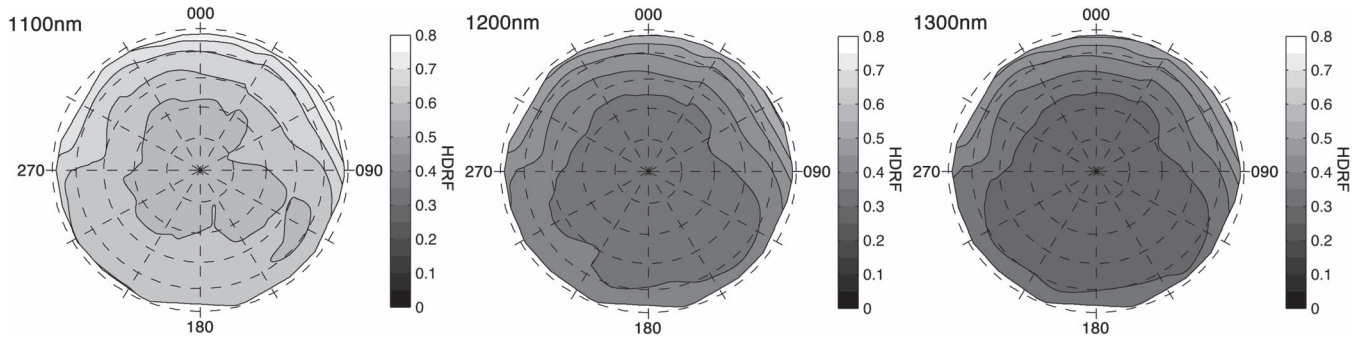

Fig. 7. Averaged HDRF for sites where the snow surface was smooth and the snow depth was over 40 cm. The dashed lines are separated by 10° in zenith and 30° in azimuth; the sun intersects each plot from 180° azimuth index. The average solar zenith angle was 82°.

a correction was then applied to the distribution in postprocessing. The correction is not valid for heterogeneous sites with roughness elements; as such, no correction for changes in solar azimuth was applied for S2 and S3. To account for the change in global irradiance during a measurement owing to the change in the solar zenith angle, a correction determined from the quotient of the radiance recorded by each foreoptic and the global irradiance recorded near simultaneously (less than 2 s) by an integrating cosine irradiance collector positioned on top of the GRASS frame was applied.

IV. Results and Discussion

In total, 11 sites were sampled during the field campaign; five sites were omitted due to the presence of cumulus or cirrus cloud during the acquisition. The HDRF was averaged over sites S1, S4, and S5 and is presented in Figs. 6–8. Fig. 6 shows the HDRF in the solar principal plane, Fig. 7 shows the HDRF presented for all viewing angles, and Fig. 8 shows the HDRF as a function of wavelength compared with Painter and Dozier's measurements of snow HDRF [11]. The averaged plots are considered to be the most representative of snow surfaces at the field site that do not contain surface roughness elements. The HDRF is presented for all the individual sites, including those with surface roughness (S2 and S3) and where the snowpack was thin (S6), in Fig. 10 as a function of view angle in the solar principal plane. Sites S2 and S3 were not included in the average because they may not be fully representative of the HDRF when viewed by a sensor with a larger footprint, for the reasons discussed in Section III-E2. The HDRF for all viewing angles for S3 is given in Fig. 9, photographs of the snowpack are shown in Fig. 10, and the list of HDRF acquisition sites and snow pit data is presented in Table I.

A. Averaged HDRF for Smooth Surfaces

The relative standard deviation in the HDRF for the averaged sites (S1, S4, S5) was less than 10% for viewing angles outside of the forward scattering peak, implying good agreement in the measurements at sites where the snowpack was thick and the snow surface was smooth.

1) HDRF Variation With Viewing Angle: The variation in the HDRF in the solar principal plane for the averaged sites (S1, S4, S5) (see Fig. 6) was minimal for wavelengths shorter than 700 nm, but strongly increased with wavelength. For example, at 1300 nm, the HDRF increased from 0.22 ± 0.01 at the nadir view position to 0.42 ± 0.17 at 45° in the forward direction in the solar principal plane, whereas at 700 nm, there was no detectable increase in the HDRF over the same viewing angle range. The extent of anisotropy in the HDRF can be described using the ratio of maximum to minimum HDRF values over all the viewing angles measured (ANIX) [see (5)] [12]. For the wavelength range 400–1300 nm, the ANIX value steadily increased with wavelength, from a minimum of 1.1 at 400 nm to 1.4 at 1100 nm, and then sharply increased to a maximum of 2.4 at 1260 nm. The increase in anisotropy in the HDRF with wavelength for snow has been observed in previous studies for different solar zenith angles (see [11]–[13]) and is the consequence of increasing absorption of radiation with wavelength, which results in a shorter penetration depth into the snowpack and reduced scattering [38]. Greater anisotropy

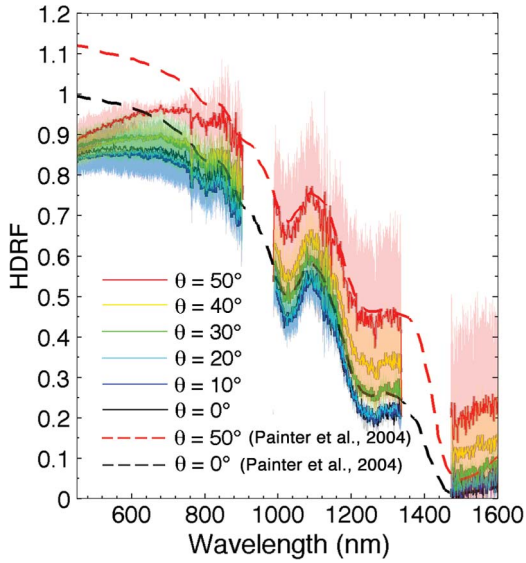

Fig. 8. Averaged HDRF with wavelength for sites where the snow surface was smooth and the snow depth was over 40 cm. Two regions of low signal to noise at 1400 nm and at 900 nm have been removed. The solid line denotes the averaged HDRF measurement, and the solid pale color denotes ± 1 standard deviation from the mean; the dashed lines denote the HDRF of snow in California recorded by Painter and Dozier [11] with a solar zenith angle of 47°.

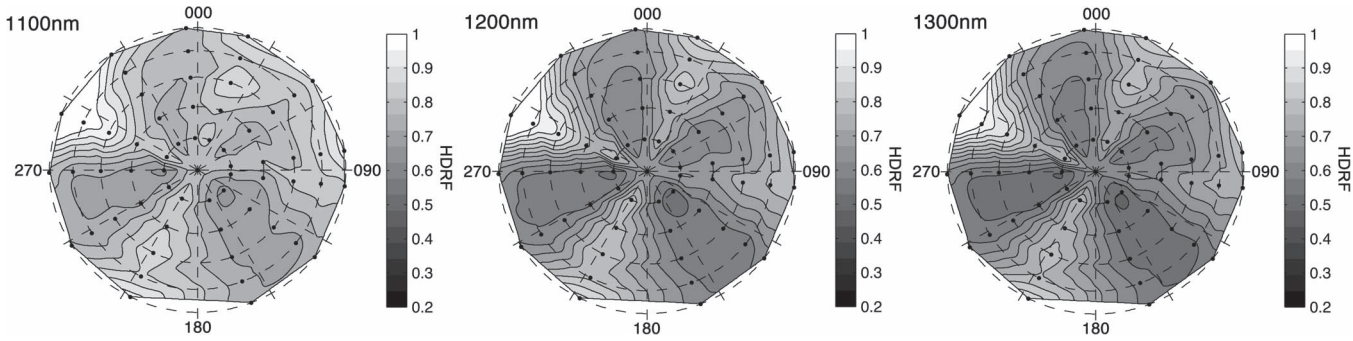

Fig. 9. HDRF for site S3 where surface roughness elements were observed and the snow depth was 9 cm. The dashed lines are separated by 10° in zenith and 30° in azimuth; the sun intersects each plot from 180° azimuth index. The average solar zenith angle was 80°.

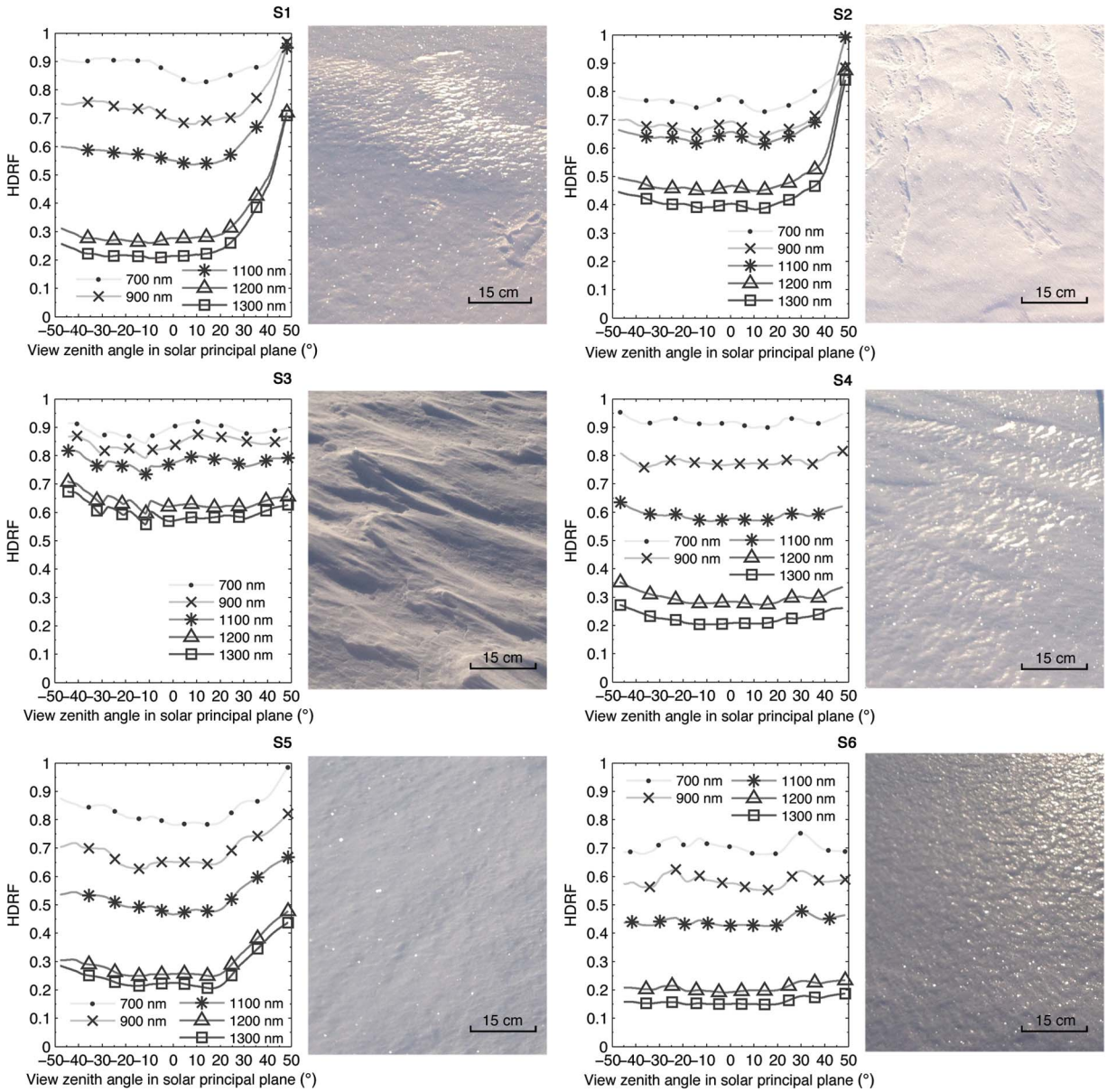

Fig. 10. HDRF in the solar principal plane (positive zenith angles correspond to the forward scattering direction) and accompanying photographs for all sites. The photographs were taken shortly after the HDRF acquisition and show snow surface roughness.

in the HDRF with wavelength is also influenced by the smaller proportion of incident diffuse irradiance at longer wavelengths, which is caused by a reduction in Rayleigh scattering [2], [24]. The standard deviation of the averaged sites in the solar principal plane was 0.17 at 1300 nm for a view angle of 45° compared with 0.01 at 1300 nm at the nadir viewing angle;

the uncertainty associated with the magnitude of the forward peak is probably the result of localized undulations in the snowpack, as well as the imperfect footprint overlap discussed in Section III-E2. Fig. 7 gives the averaged HDRF over all viewing angles measured at wavelengths 1100, 1200, and 1300 nm. The HDRF measurements in Fig. 7 are near symmetric over the solar principal plane, and the angular effects on the HDRF are strongest in the forward scattering direction and have considerably less influence for viewing angles less than 30°, particularly in the backward viewing direction. For example, for viewing angles less than 30° in the backward direction, the ANIX is 1.3 at 1300 nm and 1.1 at 1100 nm; for viewing angles less than 15° over the wavelength range 400–1300 nm, the ANIX is less than 1.1.

2) Comparison With Other HDRF Measurements: The HDRF spectra for different view angles in the solar principal plane are given in Fig. 8 and are compared with measurements made by Painter and Dozier [11] (dashed lines), who used a similar methodology to measure HDRF of snow near Mammoth Lakes, California, for solar zenith angles 47°–51°. For the wavelength range 800–1300 nm, the spectra agree well with Painter and Dozier's measurements. However, our measurements showed HDRF values up to 0.24 lower for wavelengths less than 800 nm for the same viewing angles, which is the result of absorption by impurities in the snowpack, given that the maximum mass ratio of black carbon was found to be large at our sites when compared with typical values in Svalbard. The large maximum mass ratio of black carbon in snow is the result of the proximity of the field sites to the Ny-Ålesund research base and has been reported in other studies at the same location (e.g., [39]). Black carbon has the effect of reducing the reflectance for visible wavelengths, but not in the near infrared [40], and explains the flattened spectra for the visible range compared with the measurements by Painter and Dozier [11].

The difference between the HDRF value at nadir and at 50° viewing angle gets smaller as the wavelength decreases from 700 to 500 nm in Fig. 8, whereas the difference between Painter and Dozier's measurements (the dashed lines) remains constant over this range. The decrease in HDRF with wavelength is related to non-black-carbon impurities in the snowpack, such as humic material, which is known to absorb light more strongly at shorter wavelengths [41]. The HDRF at 50° viewing angle for wavelengths greater than 1480 nm was much larger than that recorded by Painter and Dozier [11], which is explained by the larger solar zenith angle and the shorter radiation penetration depths at longer wavelengths, as, under larger solar zenith angles, there is an increased probability that a photon will exit the snowpack before it is absorbed.

B. Sites With Surface Roughness

The HDRF was recorded for two sites that contained surface roughness elements, with the largest elements observed at site S3; the HDRF over all viewing angles for S3 is given in Fig. 9. The HDRF was most anisotropic at site S3, which had the largest ANIX values of 2.8 at 1300 nm and 1.3 at 400 nm, although no forward scattering peak was observed at S3 for any wavelength, and the HDRF was strongly asymmetric with respect to the solar principal plane (with differences of up to 28% of the mean HDRF value), indicating that the roughness elements reduced scattering in the forward direction. The average HDRF value for all viewing angles at S3 was 0.6 at a wavelength of 1300 nm, compared with 0.3 at 1300 nm for averaged sites (S1, S4, and S5). S2, which exhibits some small-scale roughness elements, showed an increase in the average HDRF of all viewing angles of 0.2 at 1300 nm compared with the averages of S1, S4, and S5. There are two explanations for the increase in HDRF in the infrared region of the spectrum at S2 and S3: either a difference in grain size in the surface layer or a change in the effective solar zenith angle as a result of the surface roughness elements [42]. The data available do not indicate what is the dominant cause for the observed effect at sites S2 and S3 because grain size was not recorded in the surface layer and because of possible errors introduced as a result of the limited footprint size and the imperfect overlap, as discussed in Section III-E2. However, the roughness elements observed at S2 and S3 highlight the potential influence of surface roughness on the HDRF, as well as the importance of sampling surface roughness in order to obtain a representative HDRF, particularly at large solar zenith angles.

V. Conclusion

The HDRF of Arctic snow has been measured at large solar zenith angles (79°–85°) for six sites near the international research base in Ny-Ålesund, Svalbard, in Spring 2013. The measurements were made with the goniometric system GRASS, over the viewing angles 0°–50° and the azimuth angles 0°–360°. The variation of the HDRF values showed good consistency between sites for backward and near-nadir viewing angles with a relative standard deviation of less than 10% for sites where the snow surface was smooth and the snow depth was greater than 40 cm. The averaged HDRF showed good symmetry with respect to the solar principal plane and exhibited a forward scattering peak that was strongly wavelength dependent, with a greater than a factor of 2 increase in the ratio of maximum to minimum HDRF values over the wavelength range 400–1300 nm. The angular effects on the HDRF had minimal influence for viewing angles less than 15° in the backward viewing direction for the averaged sites, with a ratio of maximum to minimum HDRF values of less than 1.1 over the wavelength range 400–1300 nm. The averaged sites agreed well with another study of snow HDRF at a different location for infrared wavelengths, but showed differences of up to 0.24 in the HDRF for the visible wavelength range, owing to light-absorbing impurities in the snowpack, which were measured and were found to be large compared with background levels for Svalbard. The strongest anisotropy in the HDRF measurements was observed for a surface that contained the largest roughness elements, with a ratio of maximum to minimum values of up to 2.8 at a wavelength of 1300 nm. The HDRF showed no forward peak and was strongly asymmetric over the solar principal plane for the site with the largest roughness elements. However, a full explanation for the observed effect of macroscale surface roughness requires a larger footprint area and improved pointing accuracy, in order to

eliminate possible errors owing to the limited footprint size and the imperfect overlap. The measurements show the potential influence of snow surface roughness on the HDRF at large solar zenith angles and highlight the importance of sampling multiple surface types to obtain measurements of HDRF that are representative at the larger spatial scale.

ACKNOWLEDGMENT

The authors would like to thank NERC FSF for the equipment loan (662.1112), the NERC Arctic Office, Kings Bay AS, and, in particular, N. Cox at the British Antarctic Survey, for providing invaluable support in planning, logistics, and assistance with measurements.

REFERENCES

[1] G. Schaepman-Strub, M. E. Schaepman, T. H. Painter, S. Dangel, and J. V. Martonchik, "Reflectance quantities in optical remote sensing—Definitions and case studies," *Remote Sens. Environ.*, vol. 103, no. 1, pp. 27–42, Jul. 2006.

[2] T. C. Grenfell, S. G. Warren, and P. C. Mullen, "Reflection of solar radiation by the Antarctic snow surface at ultraviolet, visible, and near-infrared wavelengths," *J. Geophys. Res.*, vol. 99, no. 9, p. 18669, Sep. 1994.

[3] X. Qu and A. Hall, "Surface contribution to planetary albedo variability in cryosphere regions," *J. Climate*, vol. 18, no. 24, pp. 5239–5252, Dec. 2005.

[4] M. G. Flanner, K. M. Shell, M. Barlage, D. K. Perovich, and M. A. Tschudi, "Radiative forcing and albedo feedback from the Northern Hemisphere cryosphere between 1979 and 2008," *Nat. Geosci.*, vol. 4, no. 3, pp. 151–155, Jan. 2011.

[5] J. Stroeve *et al.*, "Accuracy assessment of the MODIS 16-day albedo product for snow: Comparisons with Greenland in situ measurements," *Remote Sens. Environ.*, vol. 94, no. 1, pp. 46–60, Sep. 2005.

[6] T. H. Painter *et al.*, "Retrieval of subpixel snow covered area, grain size, and albedo from MODIS," *Remote Sens. Environ.*, vol. 113, no. 4, pp. 868–879, Apr. 2009.

[7] C. B. Schaaf *et al.*, "First operational BRDF, albedo nadir reflectance products from MODIS," *Remote Sens. Environ.*, vol. 83, no. 1, pp. 135–148, Nov. 2002.

[8] M. Kuhn, "Bidirectional reflectance of polar and alpine snow surfaces," *Ann. Glaciol*, vol. 6, pp. 164–167, 1985.

[9] D. K. Hall, J. L. Foster, and A. T. C. Chang, "Reflectance of snow measured in situ and from space in sub-Arctic areas in Canada and Alaska," *IEEE Trans. Geosci. Remote Sens.*, vol. 30, no. 3, pp. 634–637, May 1992.

[10] Z. Jin and J. Simpson, "Anisotropic reflectance of snow observed from space over the Arctic and its effect on solar energy balance," *Remote Sens. Environ.*, vol. 75, no. 1, pp. 63–75, Jan. 2001.

[11] T. H. Painter and J. Dozier, "Measurements of the hemispherical-directional reflectance of snow at fine spectral and angular resolution," *J. Geophys. Res.*, vol. 109, no. 18, Sep. 2004, Art. ID. D18115.

[12] C. S. Bourgeois, P. Calanca, and A. Ohmura, "A field study of the hemispherical directional reflectance factor and spectral albedo of dry snow," *J. Geophys. Res.*, vol. 111, no. 20, pp. 1984–2012, Oct. 2006.

[13] S. R. Hudson, S. G. Warren, R. E. Brandt, T. C. Grenfell, and D. Six, "Spectral bidirectional reflectance of Antarctic snow: Measurements and parameterization," *J. Geophys. Res.*, vol. 111, no. 18, pp. 1–19, Sep. 2006.

[14] S. G. Warren, R. E. Brandt, and P. Hinton, "Effect of surface roughness on bidirectional reflectance of Antarctic snow," *J. Geophys. Res.*, vol. 103, no. 11, pp. 25789–25807, Jun. 25, 1998.

[15] J. I. Peltoniemi, S. Kaasalainen, J. Naranen, L. Matikainen, and J. Piironen, "Measurement of directional and spectral signatures of light reflectance by snow," *IEEE Trans. Geosci. Remote Sens.*, vol. 43, no. 10, pp. 2294–2304, Oct. 2005.

[16] A. Marks *et al.*, "Characterisation of the HDRF (as a proxy for BRDF) of snow surfaces at Dome C, Antarctica, for the inter-calibration and inter-comparison of satellite optical data," *Remote Sens. Environ.*, vol. 158, pp. 407–416, Mar. 2015.

[17] J. Liu *et al.*, "Validation of Moderate Resolution Imaging Spectroradiometer (MODIS) albedo retrieval algorithm: Dependence of albedo on solar zenith angle," *J. Geophys. Res.*, vol. 114, no. 1, Jan. 2009, Art. ID. D01106.

[18] C. Miesch, X. Briottet, and Y. Kerr, "Bidirectional reflectance of a rough anisotropic surface," *Int. J. Remote Sens.*, vol. 23, no. 15, pp. 3107–3114, Jan. 2002.

[19] K. Kuchiki, T. Aoki, M. Niwano, H. Motoyoshi, and H. Iwabuchi, "Effect of sastrugi on snow bidirectional reflectance and its application to MODIS data," *J. Geophys. Res.*, vol. 116, no. 18, Sep. 2011, Art. ID. D18110.

[20] H. Pegrum-Browning, N. Fox, and E. Milton, "The NPL Gonio rAdiometric spectrometer system (GRASS)," in *Proc. Remote Sens. Photogramm. Soc. Conf.*, Sep. 2008, pp. 1–3.

[21] A. H. Strahler and J. Muller, "MODIS BRDF/Albedo Product: Algorithm theoretical basis document version 5.0," *MODIS BRDF*, Oct. 1999, pp. 1–53.

[22] F. E. Nicodemus, J. C. Richmond, J. J. Hsia, I. W. Ginsberg, and T. Limperis, "Geometrical considerations and nomenclature for reflectance," U.S. Nat. Bureau Standards, Washington, DC, USA, p. 52, Oct. 1977.

[23] E. J. Milton, M. E. Schaepman, K. Anderson, M. Kneubuhler, and N. Fox, "Progress in field spectroscopy," *Remote Sens. Environ.*, vol. 113, pp. S92–S109, Sep. 2009.

[24] A. I. Lyapustin and J. L. Privette, "A new method of retrieving surface bidirectional reflectance from ground measurements: Atmospheric sensitivity study," *J. Geophys. Res.*, vol. 104, no. 104, pp. 6257–6268, Mar. 1999.

[25] H. Pegrum, N. Fox, M. Chapman, and E. Milton, "Design and testing a new instrument to measure the angular reflectance of terrestrial surfaces," *Proc. IEEE Int. Symp. Geosci. Remote Sens.*, 2006, pp. 1119–1122.

[26] D. C. Williams, "Establishment of absolute diffuse reflectance scales using the NPL Reference Reflectometer," *Anal. Chim. Acta*, vol. 380, no. 2, pp. 165–172, Nov. 1999.

[27] C. J. Chunnilall, A. J. Deadman, L. Crane, and E. Usadi, "NPL scales for radiance factor and total diffuse reflectance," *Metrologia*, vol. 40, no. 1, pp. 192–195, Feb. 2003.

[28] S. Sandmeier, C. Muller, B. Hosgood, and G. Andreoli, "Sensitivity analysis and quality assessment of laboratory BRDF data," *Remote Sens. Environ.*, vol. 64, no. 2, pp. 176–191, May 1998.

[29] R. D. Jackson, T. R. Clarke, and M. S. Moran, "Bidirectional calibration results for 11 Spectralon and 16 BaSO4 reference reflectance panels," *Remote Sens. Environ.*, vol. 40, no. 3, pp. 231–239, Jun. 1992.

[30] F. J. J. Clarke and D. J. Parry, "Helmholtz reciprocity: Its validity and application to reflectometry," *Lighting Res. Technol.*, vol. 17, no. 1, pp. 1–11, Mar. 1985.

[31] C. P. Ball *et al.*, "Effect of polytetrafluoroethylene (PTFE) phase transition at 19 °C on the use of Spectralon as a reference standard for reflectance," *Appl. Opt.*, vol. 52, no. 20, pp. 4806–4812, Jun. 2013.

[32] M. de Berg, O. Cheong, M. Kreveld, and M. Overmars, " *Computational Geometry: Algorithms & Applications*," Berlin, Germany: Springer-Verlag, 2008.

[33] M. Morys *et al.*, "Design, calibration, and performance of MICROTOPS II handheld ozone monitor and Sun photometer," *J. Geophys. Res.*, vol. 106, no. 13, pp. 14573–14582, Jan. 2001.

[34] C. Fierz *et al.*, "The international classification for seasonal snow on the ground; IHP technical documents in hydrology" *IACS Contrib.*, vol. 83, pp. 1–90, Nov. 2009.

[35] S. J. Doherty, S. G. Warren, T. C. Grenfell, A. D. Clarke, and R. E. Brandt, "Light-absorbing impurities in Arctic snow," *Atmos. Chem. Phys.*, vol. 10, no. 23, pp. 11647–11680, 2010.

[36] T. C. Grenfell, S. J. Doherty, A. D. Clarke, and S. G. Warren, "Light absorption from particulate impurities in snow and ice determined by spectrophotometric analysis of filters," *Appl. Opt.*, vol. 50, no. 14, pp. 2037–2048, Mar. 2011.

[37] C. Leroux and M. Fily, "Modeling the effect of sastrugi on snow reflectance," *J. Geophys. Res.*, vol. 103, no. 11, pp. 25779–25788, Oct. 1998.

[38] S. G. Warren, "Optical properties of snow," *Rev. Geophys.*, vol. 20, no. 1, pp. 67–89, Feb. 1982.

[39] J. L. France *et al.*, "Calculations of in-snow NO2 and OH radical photochemical production and photolysis rates: A field and radiative-transfer study of the optical properties of Arctic (Ny-Ålesund, Svalbard) snow," *J. Geophys. Res.*, vol. 116, no. 4, Nov. 2011, Art. ID. F04013.

[40] S. G. Warren, "Can black carbon in snow be detected by remote sensing?," *J. Geophys. Res. Atmos.*, vol. 118, pp. 779–786. Jan. 2013.

[41] J. L. France *et al.*, "Hydroxyl radical and NOx production rates, black carbon concentrations and light-absorbing impurities in snow from field

measurements of light penetration and nadir reflectivity of onshore and offshore coastal Alaskan snow," *J. Geophys. Res.*, vol. 117, no. D14, Mar. 2012, Art. ID. D00R12.

[42] W. J. Wiscombe and S. G. Warren, "A model for the spectral albedo of snow. I: Pure snow," *J. Atmos. Sci.*, vol. 37, no. 12, pp. 2712–2733, Dec. 1980.

Christopher P. Ball (M'15) received the B.Sc. (Hons.) degree in environmental geology and the M.Sc. degree in environmental geoscience from Royal Holloway, University of London, Surrey, U.K., in 2010 and 2011, respectively. He is currently working toward the Ph.D. degree in earth science at Royal Holloway, University of London.

His Ph.D. research involves the measurement and modeling of snow and sea ice bidirectional reflectance for the calibration of Earth observing ultraviolet–visible–near-infrared satellite sensors. His Ph.D. study is in collaboration with the Earth Observation and Climate Group at the National Physical Laboratory, Teddington, U.K., and is funded by the Natural Environment Research Council.

Amelia A. Marks was born in England on September 3, 1987. She received the M.Sc. degree and the Ph.D. degree in earth science from Royal Holloway, University of London, Surrey, U.K., in 2010 and 2014, respectively.

She is currently a Research Scientist with the National Physical Laboratory, Teddington, U.K., where she works in the Earth Observation and Climate Change Group focusing on the vicarious calibration of satellite sensors.

Paul D. Green received the M.Phys. degree from The University of Manchester, Manchester, U.K., in 1998 and the Ph.D. degree from Imperial College London, London, U.K., in 2003.

From 2003 to 2011, he was a Post-Doctoral Research Associate with Imperial College London, where his research focused on infrared spectroscopy of the atmosphere, water vapor, and ice clouds to better understand the processes that controlled the energy budget of the Earth's atmosphere. Since 2011, he has been a Senior Research Scientist with the National Physical Laboratory, Teddington, U.K., working on a number of projects related to the pre- and in-flight calibration of ultraviolet–visible–near-infrared satellite sensors for Earth observation applications.

Dr. Green is a Fellow of the Royal Meteorological Society and a member of the Institute of Physics. He is also a Chartered Physicist.

Alasdair MacArthur received the P.G. Dip. degree in GIS and remote sensing from Manchester Metropolitan University, Manchester, U.K., in 2002, the M.Sc. degree in environmental decision making from The Open University, Buckinghamshire, U.K., in 2004, and the Ph.D. degree in field spectroscopy and radiative transfer modeling from The University of Edinburgh, Edinburgh, U.K., in 2012.

He is currently the Facility Manager with the Natural Environment Research Council Field Spectroscopy Facility, School of Geosciences, The University of Edinburgh and is the Chair of COST Action ES1309 OPTIMISE, a European research network of 26 countries and with over 90 scientist members. He conducts research and advises on field spectroscopy methodologies and the performance and characteristics of spectroradiometers and optical sensors for environmental remote sensing and has research interests in the optical remote sensing of Calluna-vulgaris-dominated peatlands. Previously, he worked in conservation management and planning of protected areas in Scotland.

Dr. MacArthur is a Fellow of the Royal Geographical Society.

Marion Maturilli was born in Berlin, Germany, on July 8, 1971. She received the Dipl.Met. degree in meteorology and the Ph.D. degree in physics from the Free University of Berlin, Berlin, Germany, in 1997 and 2001, respectively.

In 2001, she joined, as a Postdoctoral Fellow, the Alfred Wegener Institute, Helmholtz Centre for Polar and Marine Research, Potsdam, Germany, where she became a Senior Scientist in 2003 and is currently the Head of the meteorological observatory of the French-German Arctic Research Base in Ny-Ålesund, Svalbard. She is the Ny-Ålesund site representative in the Baseline Surface Radiation Network and the Global Climate Observing System Reference Upper-Air Network. Her research has been concerned with long-term changes in Arctic climate and surface radiation.

Nigel P. Fox received the B.Sc. degree in astronomy and physics from University College London, London, U.K., in 1981.

He is currently the Head of the Earth Observation and Climate Group and a Fellow with the National Physical Laboratory, Teddington, U.K., where, since joining, he has been responsible for the establishment and dissemination of primary optical radiation measurement scales and, in particular, pioneered the development of techniques such as laser and cryogenic radiometry. These techniques led to nearly two orders of magnitude improvement in the accuracy of many radiometric measurements and have been widely adopted by the international metrology community and resulted in the award of a Ph.D. degree. He has authored or coauthored over 120 papers. More recently, he has expanded his interests to include Earth observation and associated climate change parameters, with a particular emphasis on satellite observations. This has led to further innovation in both pre- and postlaunch calibration and validation techniques and has culminated in the design and leadership of a proposed satellite mission called TRUTHS. The novel mission concept provides fully International System of Units traceable measurements from orbit at uncertainties a factor of 10 lower than any other, which is sufficient to make benchmark measurements suitable for the detection of decadal climate change.

Dr. Fox is the Chair of the Infrared Visible and Optical Sensors subgroup of the International Committee on Earth Observation Satellites and represents the international metrology community on relevant World Meteorological Organization committees.

Martin D. King received the B.A. degree in chemistry and the D.Phil. degree from the University of Oxford, Oxford, U.K., in 1995 and 1998, respectively.

From 1998 to 2000, he was an Postdoctoral Fellow with the International Arctic Research Center, Fairbanks, AK, USA. During 2001 and 2001–2003, he was Lecturer with The University of Edinburgh, Edinburgh, U.K., and with King's College London, London, U.K., respectively. He is currently a Professor of atmospheric and cryospheric science with the Department of Earth Sciences, Royal Holloway, University of London, Surrey, U.K. His research has focused on the following: 1) optical properties of snow and sea ice; 2) the oxidation chemistry of atmospheric aerosol; and 3) the atmosphere snow/sea ice exchange of chemicals.

Prof. King is a member of the Royal Society of Chemistry and the Chair of the Environmental Chemistry Special Interest Group.